Solidification Kinetics of an Al-Ce Alloy with Additions of Ni and Mn

Jordan Roger Kozakevich *, Joshua Stroh , Dimitry Sediako , David Weiss

Posted Date: 9 May 2023

doi: 10.20944/preprints202305.0637.v1

Keywords: Solidification Kinetics; Aluminum; Cerium

Article

Solidification Kinetics of an Al-Ce Alloy with Additions of Ni and Mn

Jordan Kozakevich [1,*], Joshua Stroh [1], Dimitry Sediako [1] and David Weiss [2]

[1] High Performance Powertrain Materials Laboratory, University of British Columbia, Okanagan, 1137 Alumni Ave, Kelowna V1V 1V7, Canada; dimitry.sediako@ubc.ca

[2] Eck Industries, 1602 N 8th St, Manitowoc, WI 54220, USA; david.weiss@eckindustries.com

* Correspondence: jordan.kozakevich@ubc.ca

Abstract: Heat-treated aluminum-silicon (Al-Si)-based alloys have dominated the cast lightweight alloy industry for several decades. However, in the last decade, Al-Ce-based alloys have shown promise in replacing Al-Si alloys due to their ability to remove the need for costly heat treatments. Since the properties of Al-Ce alloys depend on the as-cast microstructure, it is important to characterize the solidification kinetics of these alloys. Therefore, this study focused on characterizing the solidification of an Al-Ce alloy with additions of Ni and Mn (nominal composition Al-12.37Ce-3.26Ni-0.94Mn-0.12Fe wt.%). The alloy was cast in a wedge mold configuration, resulting in cooling rates between 0.18 and 14.27 °C/s. SEM coupled with EDS and DSC techniques characterized the evolution rate of solid phases. The SEM/EDS data revealed that an $Al_{10}CeMn_2$ phase is present at higher cooling rates. At lower cooling rates, near the center of the casting, a primary $Al_{23}Ce_4Ni_6$ phase was more present. It was observed that up to 2.6 at. % of Mn was dissolved in this primary $Al_{23}Ce_4Ni_6$ phase, thereby removing a large portion of the available Mn for forming the $Al_{10}CeMn_2$ phase. DSC analysis showed differences in the samples' liquidus temperatures which is indicative of compositional variations. Inductively coupled plasma atomic emission spectroscopy (ICP-OES) and Scheil solidification simulations correlated the compositional differences to phase formation, which agreed with the SEM and DSC results. This experimentation provides insight into novel Al-Ce-Ni-Mn alloys and where their potential lies in industrial applications.

Keywords: solidification kinetics; aluminum; cerium

1. Introduction

With the growth of environmentally friendly technology, there is a high-demand dependency on rare earth (RE) element mining. RE elements such as neodymium, praseodymium, dysprosium, and samarium are used for high-performance magnets in applications such as electric cars and wind turbines [1–3]. However, the desirable RE elements typically comprise approximately 25% of the total material mined. The remaining 75% is discarded as a by-product and has little industrial relevance [4]. Of the RE elements discarded, cerium (Ce) is the most abundant at 38% [5]. The usefulness of Ce, however, has been researched throughout the 20th century concerning alloying aluminum (Al) to help with issues of insufficient thermal stability. For example, Belov et al. [6], in 1999, conducted elevated temperature experiments with several Al alloys with additions of Ce and nickel (Ni). Targeting 350 °C, Belov and his colleagues found that an Al-12Ce-5Ni (wt.%) alloy had a 75% increase in UTS over a conventional Al-Si alloy (339) used at the time. However, this research was not continued due to the high cost of Ni and the lack of a Ce supply chain. That is, until the demand for high-performance magnets experienced a dramatic increase, resulting in an abundance of available Ce supply.

This abundance has captured the interest of researchers investigating how to improve the efficiency of internal combustion engines by creating thermally stable lightweight alloys for next-generation automotive powertrains [7–11]. A clear emergence from all this research is the potential for the Al-Ce-based alloying system to be a fundamental pillar of high-performance Al alloys that can

operate in applications that require excellent thermal stability above 200 °C [12–16]. Extensive research has gone into the fundamentals of the Al-Ce binary system to understand the platform from which a new alloying system can be structured. The solidification characteristics and phase analysis of hypoeutectic [17,18], eutectic [13,18–20], and hypereutectic [17–19,21] binary alloy compositions revealed that the $Al_{11}Ce_3$ phase has excellent castability and thermal stability up to 500 °C. In a hypereutectic composition, primary $Al_{11}Ce_3$ formation occurs. If the composition of Ce exceeds 16 wt. % the primary phase begins to crack because of the large coefficient of thermal expansion discrepancy [7]. Therefore, most studies focus on the eutectic composition to avoid any possible decrease in mechanical properties. These eutectic alloys precipitate a lamellae Al-$Al_{11}Ce_3$ phase that can retain up to 80% of its hardness when exposed to 500 °C for 168 h [13,20,22]. For comparison, the Al-Si eutectic composition only retains ~50% of its hardness when exposed to the same test [20]. This evidence justifies building an elevated-temperature Al alloy system based on the Al-Ce binary system. The current major drawback of the Al-Ce systems is that the lamellae Al-$Al_{11}Ce_3$ eutectic phase does not provide sufficient precipitate strengthening benefits for next-generation powertrain applications.

This lack of strength of the Al-Ce eutectic phase brings relevance back to the research done by Belov et al. [6], where it was found that additions of Ni enhance the strength of these alloys. Although the testing parameters in the 1999 study are not rigorous enough to meet today's automotive industry demands, they provide insight into how minor alloy elements can be used to add strength to the Al-Ce system. Sims et al. [21] drew inspiration from Belov and his colleagues and investigated two higher-order Al-Ce-based alloys with magnesium (Mg) additions. The alloys under investigation are Al-12Ce-0.4Mg and Al-12Ce-4Si-0.4Mg (wt. %). It was concluded that the Al-Ce-Mg alloy in an as-cast state exhibits a UTS and YS of 200.6 and 78.6 MPa, respectively, while the Al-Ce-Si-Mg alloy exhibits 252.3 and 128.2 MPa, respectively, when heat treated to a T6 temper. These alloys were only tested at ambient temperature but showed comparable strength with alloys such as T6 A356. Weiss et al. [23] took it a step further and tested two Al-Ce-Mg alloys, each with 8 wt. % Ce but differing in Mg content (7 vs. 10 wt. %). Both alloys were tested at ambient temperature and 260 °C. The alloy containing 7 wt.% magnesium exhibited a UTS and YS of 195 and 151 MPa, respectively. The alloy with 10 wt.% magnesium exhibited a UTS and YS of 227 and 186 MPa, respectively. When tested at 260 °C, the 7 wt.% Mg alloy retained 69% of its UTS and 80% of its YS. The alloy containing a larger amount of Mg retained 60% of its UTS and 70% of its YS. It is worth noting that these alloys were not conditioned (i.e., exposed to 260 °C for an extended period) before testing; therefore, it is expected that the alloys would perform slightly worse than expected if exposed to powertrain conditions for an extended period. It was also found in the study by Weiss et al. that the alloys were non-responsive to heat treatments aside from homogenization having a positive effect on alloys with high Mg content. Since these Al-Ce-based alloys are typically not heat treatable, they depend heavily on their solidification kinetics for their respective mechanical properties. The previous studies cited here do not account for the alloys' solidification kinetics, but it significantly impacts the mechanical properties of the alloys. This solidification rate-dependency of Al-Ce alloys removes the time and resource-consuming heat treatments from the production process. Nguyen et al. [24] and Salonitis et al. [25] predict that removing necessary heat treatments from Al alloy production alone could save 425,000–675,000 MWh annually. Along with the reduced production cost, decreasing this amount of energy for the manufacturing chain would drastically reduce the ecological footprint of the automotive industry.

Recently, Kozakevich et al. [10,14] investigated the interplay between cooling rates, microstructures and mechanical properties of an Al-Ce-Ni-Mn alloy designed for elevated temperature applications. The alloy was cast in a wedge mold configuration to investigate the effects of different cooling rates on the material's properties. The alloy exhibited a UTS and YS at ambient temperature ranging from 107 to 131 MPa and 64 to 81 MPa, respectively. At 250 °C, the alloy retained 75 to 83% of its UTS and 73 to 97% of its YS, even after conditioning at 250 °C for 150 h. The variation in tensile strength and tensile retention at 250 °C was highly dependent on the solidification kinetics of the alloy. Scanning electron microscopy (SEM) and energy-dispersive x-ray spectroscopy (EDS) revealed that the volume fraction, size, and morphology of the five phases found, α-Al, $Al_{23}Ce_4Ni_6$,

Preprints (www.preprints.org) | NOT PEER-REVIEWED | Posted: 9 May 2023 doi:10.20944/preprints202305.0637.v1

$Al_{11}Ce_3$, $Al_{10}CeMn_2$, and $Al_{20}CeMn_2$, were highly dependent on the solidification kinetics and induced directional solidification.

To better understand the solidification kinetics of the Al-Ce-Ni-Mn alloy, differential scanning calorimetry (DSC) was done on four samples from critical areas of the wedge mold in [26] (these results are summarized further in Section 3.2 of this paper). The experiment concluded that further investigation into the solidification kinetics of this alloy is warranted; a better understanding would enable a broader utilization of the alloy for various elevated-temperature applications in the automotive industry.

Therefore, the present work aims to develop a more comprehensive understanding of the alloy's solidification kinetics by performing more in-depth studies on the same samples from [26] and wedge mold casting from [10,14]. The Al-Ce-Ni-Mn alloy's solidification kinetics, microstructure, and directional solidification-induced composition variances are examined using thermodynamic simulation software, SEM, EDS, optical microscopy, DSC thermal analysis, and inductively coupled plasma-optical emission spectroscopy (ICP-OES).

2. Materials and Methods

The Al-Ce-Ni-Mn ingots used in this research were provided by Eck Industries Inc., Manitowoc, Wisconsin. The alloy was melted down in an electrical resistance furnace under argon coverage and then cast in a steel wedge mold. The samples, their locations, and other relevant information are given in Figure 1. A comprehensive description of the preliminary results and details of the casting process is described in [10]. The main casting parameters were that the alloy was poured at 700 °C, and the wedge mold was preheated to 250 °C.

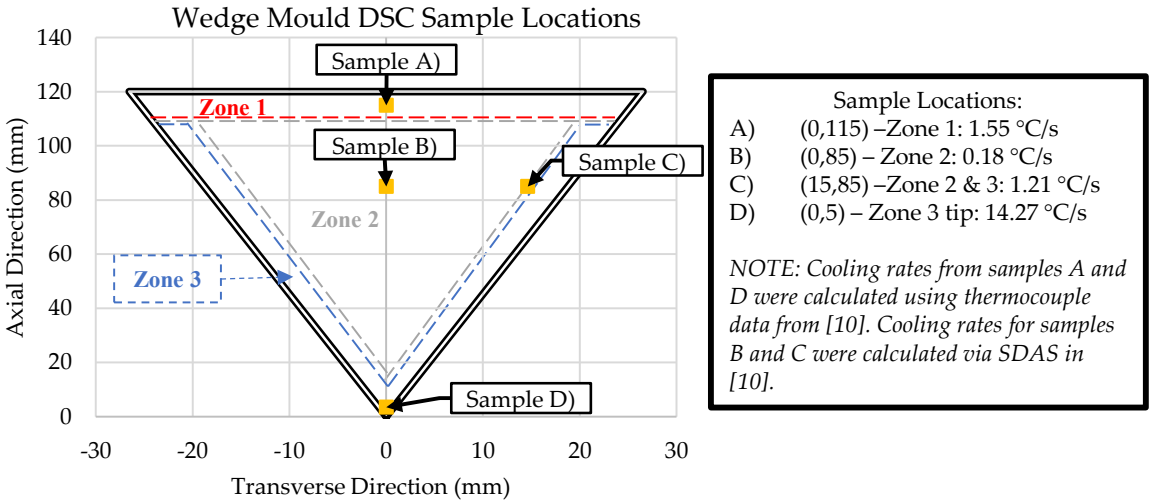

Figure 1. Sample details for SEM/EDS, DSC, and ICP-OES analysis.

The zones in Figure 1 represent regions with unique microstructures throughout the wedge mold casting. Samples were taken from critical points within the wedge mold to understand the solidification kinetics of these zones. The critical point in zone 1 (sample A) was at the top-center of the wedge mold, where a thermocouple was placed during casting. This sample gives us an exact cooling rate of the sample to compare to the follow-up DSC and ICP-OES experiments. Similarly, sample D was taken from the thermocouple placement in zone 3 for the same reasoning.

Two samples from zone 2 were taken. The first (sample B) was from the center, and the second (sample C) was at the interface between zones 2 and 3. Both samples were taken at the same axial position (85 mm) but 15 mm apart in the transverse direction. The center of zone 2 (sample B) gives the lowest cooling rate (0.18 °C/s). The interface between zone 2 and 3 (Sample C) provides insight into the transition between the initial skin developed right after pouring (high cooling rates) and the center of the wedge mold (lowest cooling rates).

Preprints (www.preprints.org) | NOT PEER-REVIEWED | Posted: 9 May 2023 doi:10.20944/preprints202305.0637.v1

Metallography samples were mounted and prepared according to ASTM E3-11 specifications [27]. Mounting was done in 2-part fast-curing acrylic. After mounting, the samples were sequentially ground with 400, 600, and 1200 silicon carbide abrasive paper and then polished sequentially with 9, 6, 3, and 1 µm diamond abrasive suspension paste. The final polish was done with 0.6 µm basic colloidal silica diamond polishing lubricant with a pH of 9.

Once the samples were prepared, optical microscopy was used to measure the secondary dendrite arm spacing (SDAS). SDAS measurements were taken with a VHX-7000 series KEYENCE digital microscope according to method E outlined in [28], which consisted of measuring between two secondary dendrites parallel to the primary arm. A minimum of 50 measurements were taken for each sample to ensure measurement and standard deviation accuracy. An example of these measurements is shown in Figure 2.

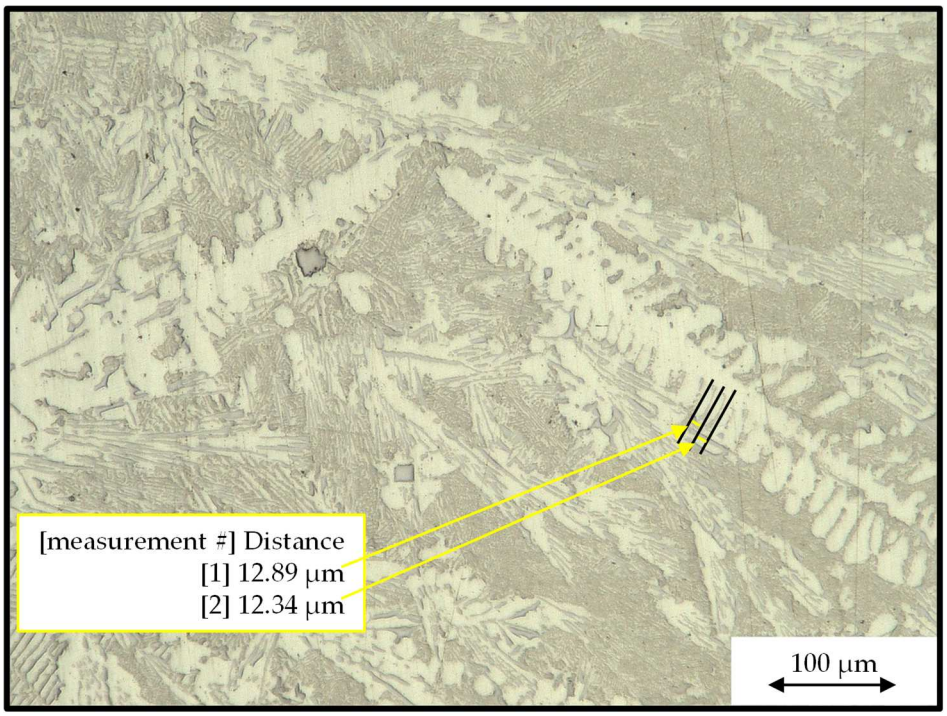

Figure 2. An optical micrograph showing how SDAS measurements were taken.

SDAS measurements were then used in Equation 1, taken from [10], which is specific to this material. Utilizing this equation allowed for calculating cooling rates where thermocouples were absent during casting (i.e., samples B and C).

$$SDAS = 11.65 * (CR)^{-0.35} \text{ [10]} \quad (1)$$

A Mira 3 XMU, TESCAN field emission gun SEM was utilized to collect micrographs of the alloy's microstructure. A Cressington 208 HR sputter coater was used to coat the sample in a 5 µm platinum (Pt) layer to enhance conductivity and reduce charging effects and heating of the samples. The SEM was operated at an accelerating voltage of 20 kV to take the micrographs. After the micrographs were collected, Oxford Instruments Aztec data acquisition and processing software equipped with an 80 mm^2 Oxford EDS detector were utilized to characterize the compositions of each phase. EDS point analysis was used to identify the atomic percentages of phases. At least 30 point scans per phase were taken to identify the atomic percentage. The EDS data and phase morphologies were compared to the literature to determine each phase's stoichiometry.

A NETZSCH STA 449F3 heat flux DSC thermal analysis instrument was employed to understand the Al-Ce-Ni-Mn alloy's phase evolution as a function of temperature. The initial liquidus and solidus temperatures were determined by Scheil ThermoCalc™ simulations to be 733 °C and 632 °C, respectively. Therefore, the temperature range of the DSC experiment was set from 20 to 750 °C.

Preprints (www.preprints.org) | NOT PEER-REVIEWED | Posted: 9 May 2023 doi:10.20944/preprints202305.0637.v1

The heating and cooling rate was selected to be 10.00 °C/min (~0.17 °C/s) based on similar studies previously conducted on Al-Ce alloys [18,29]. Each sample was 0.020 +/- 0.003 g and taken from the locations outlined in Figure 1. Samples from the original ingot material were also extracted and tested. A sample size of 0.020 g has been proven to give the most accurate results for micro-scale DSC thermal analysis [30]. Each sample was heated and cooled three times, and the results were averaged.

The results of the DSC experiment give insight into solidification kinetic specifics like solidus, liquidus, and latent heat of fusion of the eutectic reaction. Solidus and liquidus temperatures are determined by extrapolating the tangent reaction rate near the tip of the characteristic peak and projecting it to intersect the baseline of the DSC data [18,31,32]. Extrapolation of the onset and end temperatures of the characteristic peak is done according to ASTM E794 [32] standards. The end temperature of the characteristic peak only correlates to the liquidus if one peak is present in the results (i.e., all phases form near the eutectic temperature). Finally, the latent heat of fusion of the characteristic peak can be calculated by deriving the area under the peak.

ICP-OES was used in this study to confirm the ingot composition and identify the compositional changes that are the result of induced directional solidification. The samples of 0.1 g each were selected from six random locations of two different ingots. The samples were dissolved in a solution of HCl and NO_3 to digest while completely retaining the elements. After which, the solution is diluted to acquire the final elemental analysis. The average composition of the ingots is shown in Table 1.

Table 1. Composition of ingots in wt.% based on ICP-OES experimentation.

Al	Ce	Ni	Mn	Fe
Bal.	12.37 +/- 1.72	3.26 +/- 0.13	0.94 +/- 0.04	0.12 +/- 0.03

Following this, three samples of 0.1 g from each sample location (A, B, C, and D, identified in Figure 1) were extracted and tested via ICP-OES to determine the composition difference due to directional solidification in the wedge mold. The average of the three tests was taken as the sample composition for its specific location.

3. Results and Discussion

3.1. ThermoCalc™ Scheil Solidification

A Scheil solidification simulation was conducted using the ThermoCalcTM software based on the composition obtained from the ICP-OES analysis of the ingot material. The results are shown in Figure 3.

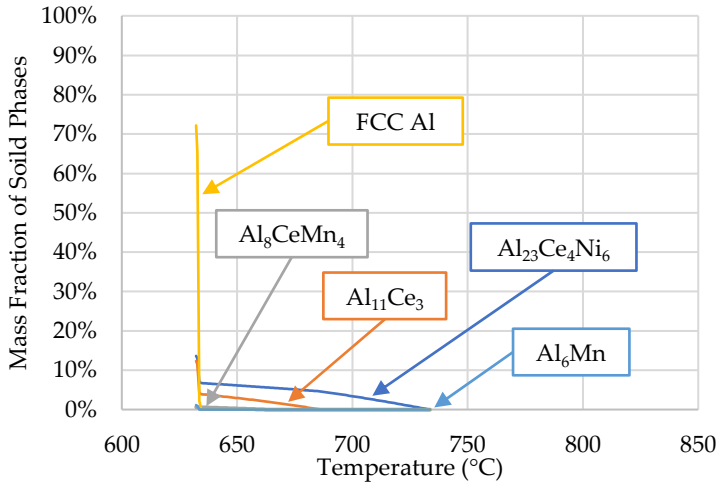

Figure 3. Scheil simulation of alloy's solidification for the composition presented in Table 1.

Preprints (www.preprints.org) | NOT PEER-REVIEWED | Posted: 9 May 2023 doi:10.20944/preprints202305.0637.v1

The phases predicted by ThermoCalc™ were α-Al (FFC Al), $Al_{23}Ce_4Ni_6$, $Al_{11}Ce_3$, Al_8CeMn_4, and Al_6Mn. The presence of these phases, except for the Al_6Mn phase, was confirmed via SEM/EDS in [10]. Limited research is available on the $Al_{23}Ce_4Ni_6$ phase concerning its solidification kinetics. In the early 2000s, Gout et al. [33] concluded that the $Al_{23}Ce_4Ni_6$ phase crystalizes in the monoclinic space group C2/m, the cell parameters for which are a = 16.042(8), b = 4.140(4), c = 18.380(8) Å, and β = 113.24(5)°. Typically, this ternary phase is accompanied by $Al_{11}Ce_3$ and Al_3Ni in ternary Al-Ce-Ni alloys; however, the results from [10] and ThermoCalc™ were in agreement that Al_3Ni does not form in the Al-Ce-Ni-Mn alloy.

In the preliminary analysis [10], when investigating the interplay between cooling rate, microstructure, and tensile properties of the current Al-Ce-Ni-Mn alloy, it was found that Al_8CeMn_4 is absent from the casting. Instead, it was replaced by $Al_{10}CeMn_2$ and $Al_{20}CeMn_2$. Over the past few years, research has been conducted on Al-Ce-Mn alloys which have focused on the Al-rich portion of this system [34–36]. Most significant to the solidification kinetics of the Al-Ce-Ni-Mn alloy described in the current study is the revised portion of the Al-rich corner of the Al-Ce-Mn ternary diagram done by Yang et al. in [34]. This revised portion of the ternary diagram shows that the $Al_{10}CeMn_2$ and $Al_{20}CeMn_2$ phases dominate earlier during solidification, with the latter phase having a slightly higher thermodynamic driving force. From this revised ternary diagram, it is expected that for the composition of the alloy under investigation (12.37% Ce, 0.94% Mn), the $Al_{10}CeMn_2$ phase would form earlier in solidification after which, at ~700 °C, the ternary Al-Ce-Mn phase would transition to $Al_{20}CeMn_2$ and $Al_{11}Ce_3$. This phenomenon is shown below in Figure 4.

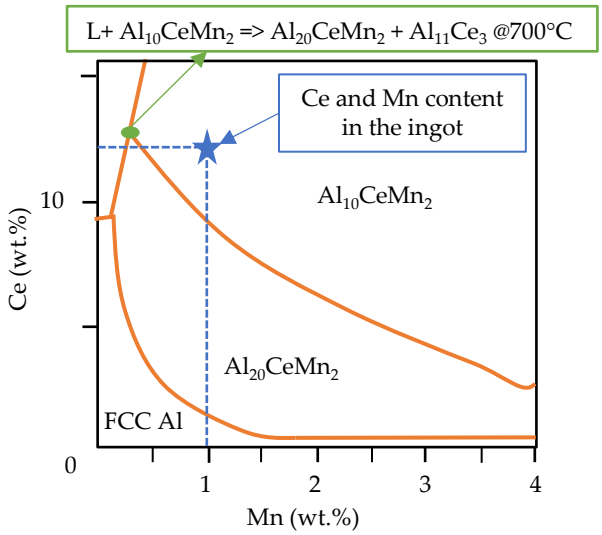

Figure 4. The modified ternary Al-Ce-Mn liquidus projection from [34] and the position of the Al-Ce-Ni-Mn alloy investigated in this study.

Aside from Scheil simulations, ThermoCalc was also used to calculate the solubility of elements in each phase. More specifically, the amount of solid solution of Mn in $Al_{23}Ce_4Ni_6$, Ni and Mn in $Al_{11}Ce_3$, Ni in Al_8CeMn_4, and Mn in the α-Al matrix was determined throughout the solidification range (734 to 632 °C). Negligible solubility was found in all cases except for Mn in the α-Al matrix, where the maximum solid solution at 632 °C was 0.4 at.%, lower than the 0.6 at.% published in binary Al-Mn literature [37,38]. However, Mondolfo's investigation into Al-Ce-Mn alloys [39] reveals that Ce reduces Mn's solid solubility in Al. The SEM/EDS data discussed in the next section shows how much Mn is present in the Al matrix and how its solubility is affected by the solidification rate of the alloy.

3.2. SEM/EDS Solidification Trends

Previously in [10], the resulting wedge casting revealed three distinct zones with varying microstructures. Figure 1 shows sample locations and how respective cooling rates were determined,

Preprints (www.preprints.org) | NOT PEER-REVIEWED | Posted: 9 May 2023 doi:10.20944/preprints202305.0637.v1

while Figure 5 below shows the microstructure at those sample locations. The phases in each zone were relatively the same and contained variations of α-Al, eutectic Al-$Al_{23}Ce_4Ni_6$, eutectic Al-$Al_{11}Ce_3$, primary $Al_{23}Ce_4Ni_6$, primary $Al_{11}Ce_3$, and $Al_{20}CeMn_2$. The $Al_{10}CeMn_2$ phase was only present in samples C and D near the wall of the casting. All Mn in samples A and B were either in solid solution in the Al matrix or $Al_{20}CeMn_2$ phase.

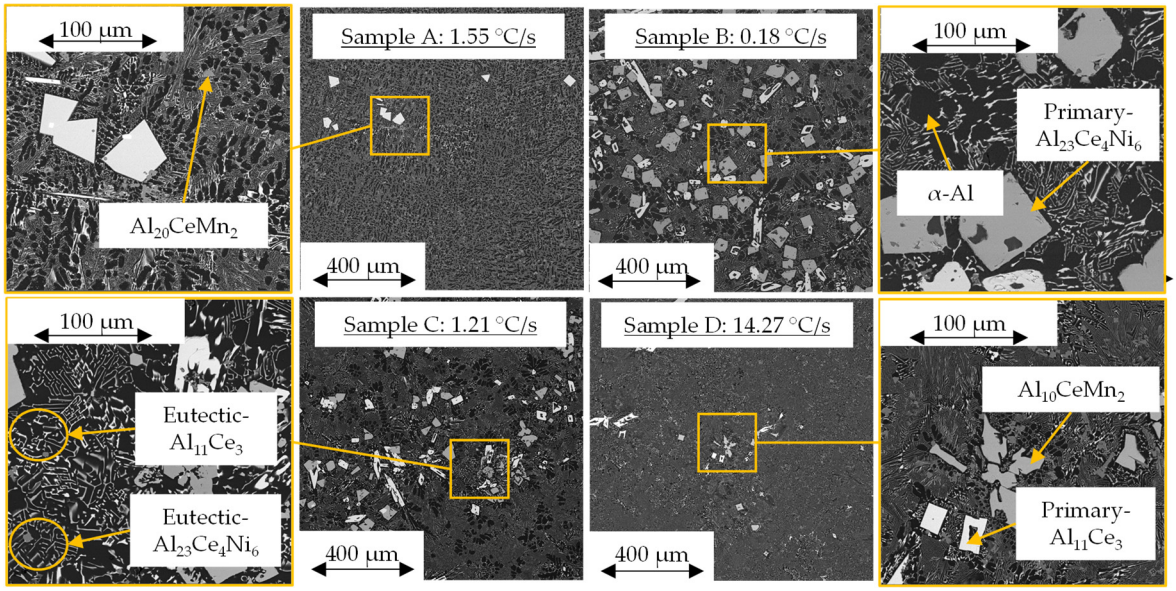

Figure 5. SEM micrographs of each sample's general microstructure.

Point scans were performed for each phase to determine the atomic composition. After this, the atomic composition was compared to published literature on similar phases to determine the correct stoichiometry of a specific phase. The atomic compositions of each phase are summarized here in Table 2.

Table 2. The atomic percentage of phases identified in the Al-Ce-Ni-Mn alloy by EDS.

Phase Identification	Element in phase (at. %)				
	Al	Ce	Ni	Mn	Fe
Matrix (α-Al)	99.77 +/- 0.21	-	-	0.23 +/- 0.21	-
$Al_{11}Ce_3$ - Primary	79.61 +/- 1.37	20.36 +/- 1.36	-	-	-
$Al_{11}Ce_3$ - Eutectic	93.43 +/- 1.42	6.41 +/- 1.53	0.16 +/- 0.37	-	-
$Al_{23}Ce_4Ni_6$ - Primary	73.37 +/- 0.57	8.19 +/- 0.11	15.77 +/- 0.34	2.56 +/- 0.06	0.01 +/- 0.05
$Al_{23}Ce_4Ni_6$ - Eutectic	89.09 +/- 3.14	3.25 +/- 0.99	6.57 +/- 1.93	1.10 +/- 0.24	-
$Al_{10}CeMn_2$	79.02 +/- 0.83	7.47 +/- 0.33	3.33 +/- 0.20	10.17 +/- 0.45	-
$Al_{20}CeMn_2$	87.99 +/- 1.00	4.20 +/- 0.27	0.32 +/- 0.35	7.50 +/- 0.77	-

The Al matrix contained an average of 0.23 at. % Mn in solid solution. Higher cooling rates near the wall (e.g., sample D) resulted in up to 0.44 at. % Mn in the matrix. As previously stated, these values are lower than the published literature [37,38] on Al-Mn alloys (~0.62 at.% Mn into α-Al). However, also mentioned above, Mondolfo's investigation into Al-Ce-Mn alloys [39] revealed that

 doi:10.20944/preprints202305.0637.v1

Ce lowers the solubility of Mn in the matrix, which explains the lower values of Mn in α-Al presented in Table 2.

$Al_{11}Ce_3$ was present in two morphologies: blocky primary and lamellae eutectic phases. These morphologies are consistent with the literature data on the binary Al-Ce alloys [17,19,20]. The primary intermetallic resides in samples B, C, and D but not at the top of the casting (sample A). The stoichiometry of the primary phase was consistent with the literature [40] and contained no Ni or Mn in a solid solution. The lamellae eutectic $Al_{11}Ce_3$ contained a trace amount of Ni (0.16 at. %) in a solid solution. Research by Tang et al. in [41] and [42] revealed between 0.6 and 1.7 at.% Ni can be dissolved into the $Al_{11}Ce_3$ phase. However, the alloys in these studies contain significantly higher Ce and Ni content, which justifies why they experienced an elevated amount of Ni in the solid solution of the $Al_{11}Ce_3$ phase.

The solubility of Ni in the eutectic phase and not the primary phase can be explained by the precipitation kinetics of the $Al_{23}Ce_4Ni_6$ phases. In the early stages of solidification (~732 °C), the primary $Al_{23}Ce_4Ni_6$ phase (also known as the τ8 phase [33,41–44]) begins to form, drawing Al and Ni out of the liquid at a higher rate than Ce. Eventually, the liquid becomes Ce enriched, and the $Al_{11}Ce_3$ primary phase begins to precipitate out of the liquid around 686 °C. Since the primary $Al_{23}Ce_4Ni_6$ phase has a high growth rate, no excess Ni can be dissolved into the primary $Al_{11}Ce_3$ phase. However, once the alloy reaches the eutectic temperature, precipitation of the lamellae Al-$Al_{23}Ce_4Ni_6$ and Al-$Al_{11}Ce_3$ phases happens simultaneously. These phases are thin and fine, and since Ni has negligible solubility in the Al matrix, the remaining Ni goes into both eutectic lamellae phases, resulting in ~0.16 at. % Ni in the Al-$Al_{11}Ce_3$ eutectic phase. However, due to the nano-scale size of the $Al_{11}Ce_3$ eutectic phase, the electron beam during EDS analysis may be penetrating the surrounding Al-matrix, thereby diluting the measurements. Therefore, the expected Ni composition in the eutectic Al-$Al_{11}Ce_3$ can be calculated based on the ratio of Ce to Ni. Since the Ce:Ni ratio is ~40:1, we can scale the 6.41 at. % Ce up to ~ 20 at. % based on our EDS data, which is consistent with the literature. Doing so scales the Ni at. % in the eutectic $Al_{11}Ce_3$ to ~ 0.509 at. %, which is closer to the values published in the literature [41,42].

Similarly, the EDS results from the $Al_{23}Ce_4Ni_6$ eutectic phase also present evidence of dilution due to the surrounding Al-matrix. When scaling the Ni:Mn ratio of the eutectic phase up to the expected composition of 15.77 at. % Ni, it is expected that ~2.6 at. % Mn can be found in the solid solution of the $Al_{23}Ce_4Ni_6$ lamellae eutectic, which is approximately the Mn content found in the primary phase. Aside from the Mn content found in the $Al_{23}Ce_4Ni_6$ phases, the amounts of Ce and Ni shown in Table 2 are consistent with the published data in [33,41–44]. The eutectic and primary phases are larger in sample B than in the other samples. This is consistent with the results presented in [14]. As shown in Table 2, both morphologies of this phase have a significant Mn solubility (~ 2.56 at. %), a phenomenon that is not currently predictable by the ThermoCalc™ software.

The same conclusion applies to both ternary Al-Ce-Mn phases in the wedge mold casting. It was found that the $Al_{10}CeMn_2$ phase has an average of 3.3 at. % Ni in solid solution, while the $Al_{20}CeMn_2$ phase contains much less (i.e., 0.32 at. %) Ni in solid solution. The $Al_{10}CeMn_2$ and $Al_{20}CeMn_2$ phases are consistent in size and morphology with those found and characterized in [34] and [35].

3.3. DSC Thermal Analysis

The SEM micrographs and EDS compositional analysis show that the phase morphologies and volume fractions within each zone of the wedge mold casting differ significantly. These factors depend on the changes in the progression of phase evolution that resulted from varying cooling rates. DSC thermal analysis was necessary to understand the phase precipitation characteristics and to gain further insight into the solidification kinetics of this alloy. Initial DSC thermal analysis was performed in [26] to show how the solidification kinetics affect the alloy's microstructure. The preliminary DSC results are shown in Figure 6 below. The indicated sample locations correspond to those in the experimental procedure section above. The solidus temperature, latent heat of fusion of the eutectic phase, and liquidus temperature were extracted from the DSC results.

Preprints (www.preprints.org) | NOT PEER-REVIEWED | Posted: 9 May 2023 doi:10.20944/preprints202305.0637.v1

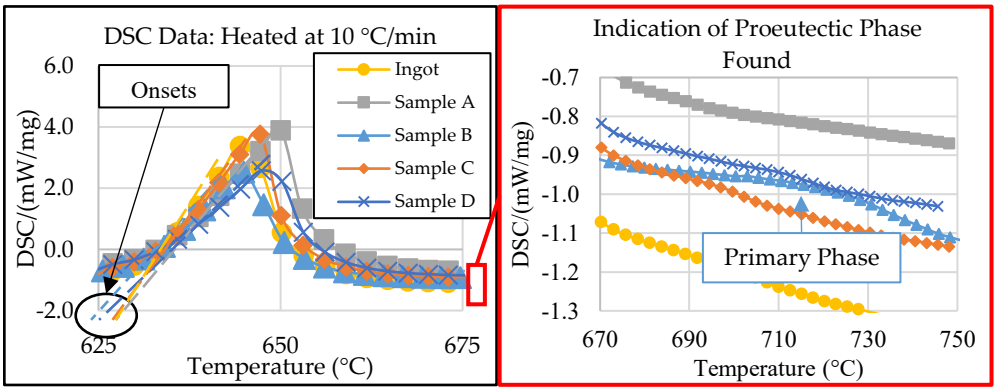

Figure 6. DSC data of all samples, modified and adapted from [26].

Figure 6 shows that all samples provide a similar solidus temperature (onset) to the 632 °C predicted by the Scheil simulation of the ingot material in ThermoCalc™, except for sample B, which is 5 °C lower [26]. The discrepancy in eutectic temperatures between sample B and the ingot suggests a compositional variance in the center of the wedge mold (zone 2). Additionally, the exploded view in Figure 6, on the right, shows evidence of primary formation in samples B, C, and D at different temperatures, suggesting compositional variations between the DSC samples. These results are consistent with the SEM micrographs.

The compositional difference between the samples shown from the initial DSC results suggests that further investigation is needed before determining if the end temperature of the eutectic reaction can be considered as the liquidus temperature for samples A, C, and D. Additional information is also needed from sample B to ensure that no other primary peak forms above 800 °C. For this reason, the determined liquidus temperature of each sample is discussed in Section 3.4 below.

Aside from the liquidus and solidus temperatures, the DSC data show the significant variance of the eutectic reaction latent heat of fusion between samples. The latent heat of fusion from DSC thermal analysis is calculated based on the energy absorbed (exothermic is identified in Figure 6) during the melting of the eutectic phase, which is then normalized by the sample's total mass. Therefore, if the samples have significantly different latent heat of fusion values, they must also have different volume fractions of eutectic phases. For example, sample B has the least amount of characteristic latent heat of fusion. In Figure 5, sample B also has the highest volume fraction of primary phases, indicating that sample B has a different composition than the original ingot. This compositional difference results from the cooling gradient induced by the wedge mold configuration. This significant cooling gradient varies the alloy's solidification kinetics, resulting in varying compositions within the critical zones of the casting. The significance of how the composition varies can be characterized via ICP-OES analysis.

3.4. ICP-OES Data

ICP-OES analysis was done to characterize the composition gradient that directly results from the solidification kinetics of the Al-Ce-Ni-Mn alloy and the directional solidification induced by the wedge mold casting configuration. The results from the ICP-OES experiments are shown in Figure 6. In Figure 6, the down arrows highlighted in red indicate the elemental percentage of change compared to the original ingot composition shown in Table 1. Green up arrows indicate increases in elemental composition based on the original ingot values.

Figure 7 shows that the ICP-OES results of samples A and C have significant decreases in Ce, Ni, and Mn compared to the original ingot composition. In turn, the Ce, Ni, and Mn concentration increase in samples B and D. The exact compositions are shown below in Table 3.

Preprints (www.preprints.org) | NOT PEER-REVIEWED | Posted: 9 May 2023 doi:10.20944/preprints202305.0637.v1

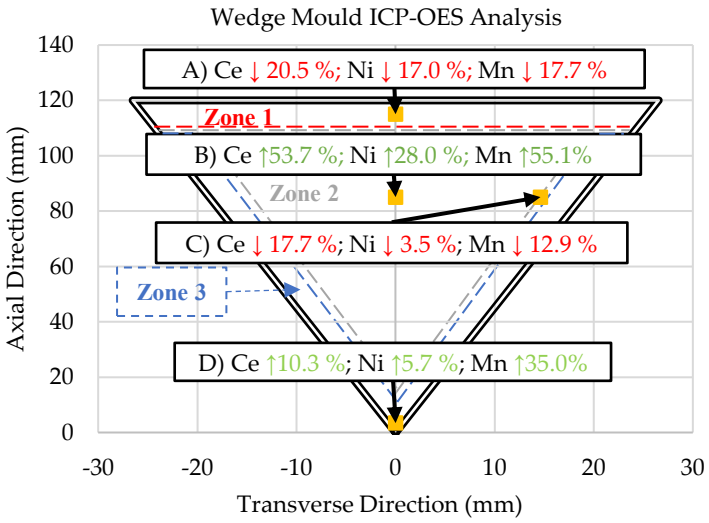

Figure 7. Summary of the wt.% changes of each sample compared to the ingot composition as determined by ICP-OES analysis of location in the wedge mold. NOTE: The up and down arrows indicate percent increase or decrease, respectively, from the original ingot composition in Table 1.

Table 3. OES-ICP data for the Ingot materials and samples A, B, C, and D (all values in wt.%).

	Al	Ce	Ni	Mn	Fe
Ingot (Reference)	Bal.	12.374 +/- 1.722	3.263 +/- 0.129	0.937 +/- 0.041	0.119 +/- 0.032
A) 1.55 °C/s	Bal.	9.842 +/- 0.185 (-20.5%)	2.707 +/- 0.027 (-17.0%)	0.771 +/- 0.016 (-17.7%)	0.0917 +/- 0.002 (-22.8%)
B) 0.18 °C/s	Bal.	19.024 +/- 0.712 (+53.7%)	4.175 +/- 0.192 (+28.0%)	1.452 +/- 0.017 (+55.1%)	0.157 +/- 0.002 (+32.0%)
C) 1.21 °C/s	Bal.	10.183 +/- 0.128 (-17.7%)	3.150 +/- 0.032 (-3.5%)	0.816 +/- 0.012 (-12.9%)	0.087 +/- 0.001 (-26.6%)
D) 14.27 °C/s	Bal.	13.652 +/- 0.104 (+10.3%)	3.450 +/- 0.028 (+5.7%)	1.264 +/- 0.015 (+35.0%)	0.157 +/- 0.001 (+32.2%)

The ICP-OES-determined compositions of each sample were used in Scheil simulations to determine the solidification kinetics of each critical zone of the wedge mold. The results of these Scheil simulations are shown in Figure 8.

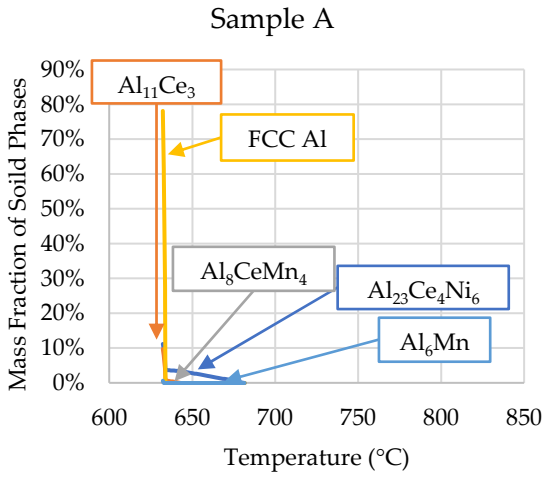

Preprints (www.preprints.org) | NOT PEER-REVIEWED | Posted: 9 May 2023 doi:10.20944/preprints202305.0637.v1

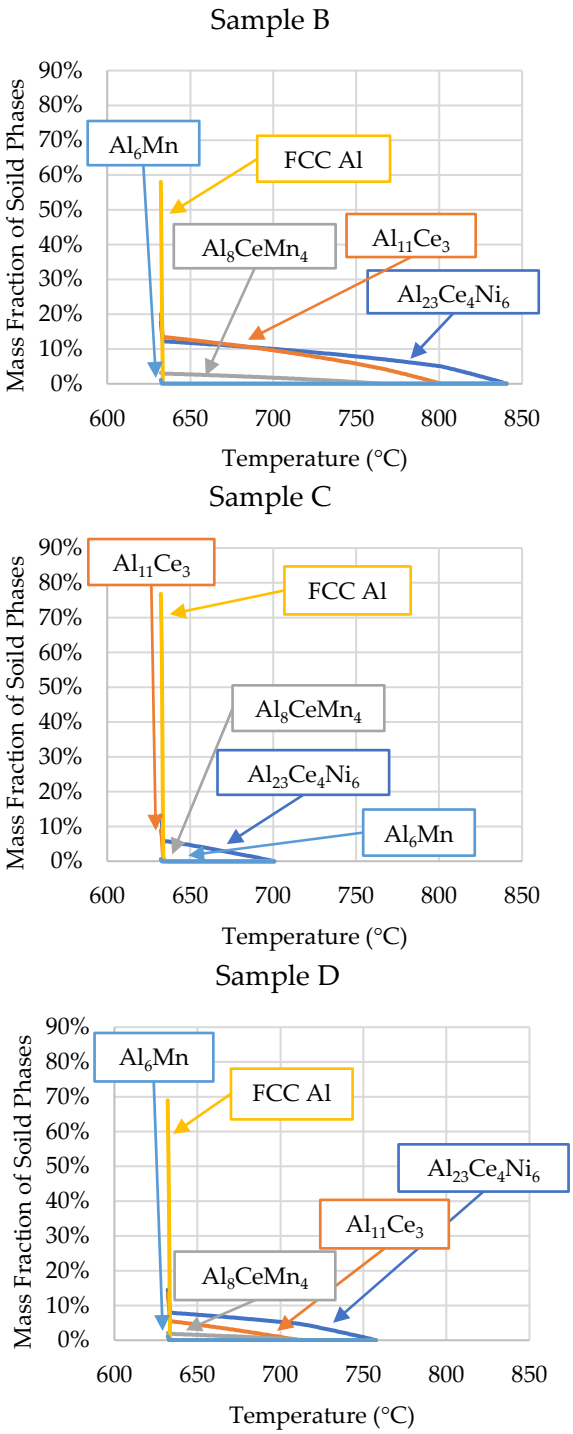

Figure 8. Scheil simulations of the alloys solidification for the compositions determined by ICP-OES analysis of each sample position (presented in Table 3).

The phase evolutions shown in Figure 8 are consistent with the SEM micrographs and DSC data. The only discrepancy is that small amounts of Al_6Mn precipitate close to the end of Scheil solidification in all the samples. However, SEM/EDS showed no presence of Al_6Mn in the casting. As mentioned, ThermoCalc™ does not account for the precipitation of $Al_{10}CeMn_2$ and $Al_{20}CeMn_2$. Instead, the software predicts the Al_8CeMn_4 phase to precipitate, which was disproved by the EDS data in Table 2.

The Scheil simulation for each sample reveals that Sample A shows the proeutectic $Al_{23}Ce_4Ni_6$ starting to precipitate at 682 °C. The software predicts 3.8 wt.% (<1 vol.%) of the primary $A_{23}Ce_4Ni_6$ phase which is consistent with the SEM micrographs. The relatively low amount of the primary

Preprints (www.preprints.org) | NOT PEER-REVIEWED | Posted: 9 May 2023 doi:10.20944/preprints202305.0637.v1

phase, coupled with the precipitation temperature being close to the eutectic temperature, explains why the phase does not register in the DSC results. It is likely that during DSC experimentation, the proeutectic formation of the $Al_{23}Ce_4Ni_6$ phase is encapsulated in the characteristic peak. Therefore, the end temperature of the characteristic peak (655 °C) from the DSC results for sample A is likely the liquidus temperature of the sample. This value is lower than the Scheil predicted value of 682 °C. The disagreement between liquidus temperatures is likely because the mass fraction of the primary phases is not significant enough for the DSC to detect the resulting reaction energy. The DSC and Scheil simulation agree that the solidus temperature of sample A is 632 °C.

The comparison between the DSC and ThermoCalc™ results is summarized in Table 4 for all samples. Table 4 shows that all samples agree with the Scheil simulation and DSC results of the solidus temperature except for sample B. The DSC results for Sample B show that the solidus temperature is 627 °C, while the Scheil simulation predicts the solidus temperature as 632 °C, a 5 °C difference. The other samples are between 1 to 3 °C off the simulated value.

Table 4. Liquidus and solidus temperatures of ICP-OES sample compositions based on Scheil simulations compared to DSC.

	Liquidus (°C)		Solidus (°C)	
	DSC	**ThermoCalc™**	**DSC**	**ThermoCalc™**
Ingot	662	734	632	632
Sample A	655	682	633	632
Sample B	-	841	627	632
Sample C	700	701	632	632
Sample D	-	758	629	632

Note: "-" indicates that the value could not be interpreted from the DSC results because it was outside the original solidification range predicted by the ingot composition and Scheil simulation.

The solidification range of sample B's ICP-OES composition is increased significantly due to the hypereutectic Ce and Ni content. Precipitation of the primary $Al_{23}Ce_4Ni_6$ phase begins at 840 °C compared to 734 °C in the ingot material, as predicted by the Scheil simulation. Since the DSC experiment on this sample only went up to 800 °C, the liquidus temperature of the alloy cannot be determined by the DSC data. However, the Scheil simulation of sample 'B's composition in Figure 8 does give insight into what exactly is happening during solidification within the wedge mold. This large solidification range and low cooling rate (0.18 °C/s) explain why the SEM micrographs of sample B show larger primary phases than the other samples. Since Sample B is from zone 2, it can be observed that when zone 3 solidifies (sample D) first at a relatively high cooling rate (14.27 °C/s), elevated amounts of Ce and Ni reside in the liquid. Excess Ni and Ce would reside in the liquid because the high cooling rate of zone 3 does not allow enough time for the primary $Al_{23}Ce_4Ni_6$ and $Al_{11}Ce_3$ phases to precipitate in significant amounts. Zone 2 begins to solidify much slower because the steel mold is now heat-soaked, resulting in significantly reduced heat flux. The slower solidification rate and elevated amounts of Ce and Ni allow for forming of large primary $Al_{23}Ce_4Ni_6$ and $Al_{11}Ce_3$ intermetallics.

Sample D's Ni and Mn content is very similar to sample B; however, the microstructure is vastly different. Figure 8 and Table 4 show that the solidification range for sample D compared to sample B is ~83 °C smaller. This smaller solidification range and a significantly higher cooling rate resulted in the precipitation of the $Al_{10}CeMn_2$ phase in sample D but not in sample B. As previously stated, the revised Al-Ce-Mn ternary diagram from Yang et al. [34] shows that the ternary $Al_{10}CeMn_2$ phase transitions to $Al_{11}Ce_3$ and $Al_{20}CeMn_2$ at 700 °C. The high cooling rates experienced in sample D do not allow enough time for this reaction to occur, trapping the $Al_{10}CeMn_2$ phase in the solid. This phenomenon is also evident in sample C at a cooling rate of 1.21 °C/s. Sample A and B had no $Al_{10}CeMn_2$ in their microstructure, which indicates that to remove this phase, an Mn content of 0.771 wt.% (or less) or a cooling rate lower than 1.21 °C/s is required.

Sample C shows good agreement of the solidus and liquidus temperature between the Scheil simulation and DSC results, as shown in Table 4. Since sample C has a composition closely resembling the ingot composition, the formation of the primary phases is contained in the DSC results. Therefore, the liquidus temperature (700 °C) can be extracted from the DSC results.

4. Conclusions

This study investigated the solidification kinetics of an Al-Ce alloy with additions of Ni and Mn when cast in a wedge mold configuration. The wedge mold configuration was determined to induce significant directional solidification, leading to large microstructure variations throughout the final cast product. When analyzing the three critical zones of the wedge mold casting via SEM/EDS, DSC Thermal Analysis, and ICP-OES, the following conclusions were made:

1. Cooling rate and directional solidification drastically affect the formation of the ternary Al-Ce-Mn phases. Cooling rates above 1.21 °C/s do not allow the $Al_{10}CeMn_2$ phase to transition to $Al_{20}CeMn_2$ + $Al_{11}Ce_3$ at 700 °C. Therefore, the Al-Ce-Ni-Mn alloy can have its mechanical properties tailored based on which Al-Ce-Mn ternary phase benefits specific applications.
2. Induced directional solidification also significantly impacts the consistency of composition throughout the final cast product. The solidification sequence must be considered when casting these novel alloys as rapidly solidified areas will lead to hypereutectic compositions in the slower cooled regions of the casting, as is evident by the ICP-OES results in this study. A hypereutectic composition and large solidification range lead to significant primary blocky $Al_{23}Ce_4Ni_6$ and $Al_{11}Ce_3$ phases, which may be desirable or undesirable, depending on the application.
3. The $Al_{23}Ce_4Ni_6$ phase has a notably higher (~2.6 at. %) Mn solubility than predicted by the ThermoCalc™ software. The same goes for the solubility of Ni in $Al_{10}CeMn_2$ (3.33 at. %) and $Al_{20}CeMn_2$ (0.32 at. %).

The comprehensive correlation between the solidification cooling rate, directional solidification-induced compositional variances, and the resulting microstructure/phase evolution provide critical insight into how this novel Al alloy can be tailored for different applications in the automotive industry.

Author Contributions: Conceptualization, J.K.; methodology, J.K. and J.S.; software, J.K.; validation, J.K. and J.S.; formal analysis, J.K.; investigation, J.K.; resources, D.S. and D.W.; data curation, J.K.; writing—original draft preparation, J.K.; writing—review and editing, J.S, D.S. and D.W.; visualization, J.K. and J.S.; supervision, D.S. and D.W.; project administration, D.S. and D.W.; funding acquisition, D.S. and D.W. All authors have read and agreed to the published version of the manuscript.

Funding: This work was supported by Eck Industries and the Mitacs International Award [Application Ref. IT23293].

Data Availability Statement: The raw and processed data required to produce these findings are available for download from Mendeley Data ["Solidification kinetics of an Al-Ce alloy with additions of Ni and Mn", https://data.mendeley.com/datasets/nmmvwn9yf4].

Acknowledgments: The authors would like to acknowledge Dr. Mark Button and Dr. Sudip Shrestha of the UBCO FiLTER laboratory for their contributions to the ICP-OES and SEM data used in this article.

References

1. Castro-Alvarez, A.; Gil Y.; Llanos, L.; Aravena, D. High performance single-molecule magnets, Orbach or Raman relaxation suppression. *Inorg. Chem. Front.* **2020,** 7, 2478–2486, https://doi.org/10.1039/d0qi00487a.
2. Goll, D.; Kronmüller, H. High-performance permanent magnets. *Naturwissenschaften* **2000,** 87, 423–438, https://doi.org/10.1007/s001140050755.
3. Hirosawa, S.; Nishino, M.; Miyashita, S. Perspectives for high-performance permanent magnets: Applications, coercivity, and new materials. *Adv. Nat. Sci. Nanosci. Nanotechnol.* **2017**, 8, https://doi.org/10.1088/2043-6254/aa597c.
4. U. S. G. Survey. Mineral commodity summaries. Available online: https://www.usgs.gov/centers/nmic/mineral-commodity-summaries (accessed 15 Jan. 2023)

5. Sims, Z. C. et al. How cerium and lanthanum as coproducts promote stable rare earth production and new alloys. *J. Sustain. Metall.* **2022**, 1225-1234, https://doi.org/10.1007/s40831-022-00562-4.
6. Belov, N.A; Naumova, E. A.; Eskin, D. G. Casting alloys of the Al-Ce-Ni system: Microstructural approach to alloy design. *Mater. Sci. Eng. A* **1999,** 271, 134–142, https://doi.org/10.1016/s0921-5093(99)00343-3.
7. Stroh, J.; Sediako, D.; Weiss, D. Development of cerium-reinforced specialty aluminum alloy with application of X-ray and neutron diffraction. *Int. J. Met.* **2021**, 15, 29–39, https://doi.org/10.1007/s40962-020-00467-6.
8. Aghaie, E.; Stroh, J.; Sediako, D.; Rashidi, A.; Milani, A. S. Improving the mechanical properties of the B319 aluminum alloy by addition of cerium. *Mater. Sci. Eng. A* **2020**, 793, 1–9, https://doi.org/10.1016/j.msea.2020.139899.
9. Kozakevich, J. R.; Stroh, J.; Sediako, D.; Weiss, D.; Loukus, A.; Vogel, S. C. Elevated temperature creep and tensile performance of extruded Mg-10Ce alloy. *J. Mater. Eng. Perform.* **2022**, 32, 2758–2765, 2022, https://doi.org/10.1007/s11665-022-06935-w.
10. Kozakevich, J. R.; Stroh, J.; Mallouhi, V.; Sediako, D.; Weiss, D. Interplay between cooling rate, microstructure, and mechanical properties of an Al-Ce-Ni-Mn alloy. *Light Met.* **2022**, 83–89, doi: https://doi.org/10.1007/978-3-030-92529-1_11.
11. Fodran, E. J. Microstructural evolution and thermal stability of Al-Ce-Ni ternary eutectic. Doctor in Philosophy, The University of Florida, Gainesville, August 2002.
12. Weiss, D. Improved high-temperature aluminum alloys containing cerium. *J. Mater. Eng. Perform.* **2019**, 28, 1903–1908, https://doi.org/10.1007/s11665-019-3884-2.
13. Czerwinski, F. Thermal stability of aluminum–cerium binary alloys containing the Al–Al11Ce3 eutectic. *Mater. Sci. Eng. A* 809, **2021**, 1–11, https://doi.org/10.1016/j.msea.2021.140973.
14. Kozakevich, J. R. Development and characterization of a novel near-eutectic Al-Ce alloy with additions of Ni and Mn for elevated temperature applications in the automotive industry. Master's Thesis, The University of British Columbia, Kelowna December 2022.
15. Stroh, J. Development of orecipitation-strengthened aluminum alloys and manufacturing processes for next generation automotive powertrains. Doctor in Philosophy, The University of British Columbia, Kelwona, April 2021.
16. Sims, Z. C. et al. High performance aluminum-cerium alloys for high-temperature applications. *Mater. Horizons* **2017**, 4, 1070–1078, https://doi.org/10.1039/c7mh00391a.
17. Stroh, J.; Sediako, D.; Weiss, D.; Peterson, V. K. In situ neutron diffraction solidification analyses of rare earth reinforced hypoeutectic and hypereutectic aluminum-silicon alloys. *Light Metals* ***2020***, 174–178, https://doi.org/10.1007/978-3-030-36408-3_24.
18. Aniolek, M.; Smith, T.; Czerwinski, F. Combining differential scanning calorimetry and cooling- heating curve thermal analysis to study the melting and solidification behavior of al-ce binary alloys. *Metals (Basel).* **2021**, 11, 1–17, 2021, https://doi.org/10.3390/met11020372.
19. Czerwinski, F.; Amirkhiz, B. S. On the Al-Al11Ce3 eutectic transformation in aluminum-cerium binary alloys. *Materials (Basel).* **2020**, 13, doi: https://doi.org/10.3390/ma13204549.
20. Czerwinski, F. A search for the eutectic system of high-temperature cast aluminum alloys. *Mater. Sci. Technol. (United Kingdom)* **2021**, 37, 683–692, https://doi.org/10.1080/02670836.2021.1940670.
21. Sims, Z. C. et al. Cerium-based, intermetallic-strengthened aluminum casting alloy: high-volume co-product development. *J. Miner. Met. Mater. Soc.* **2016**, 68, 1940–1947, https://doi.org/10.1007/s11837-016-1943-9.
22. Czerwinski, F. Thermal stability of aluminum alloys. *Materials (Basel).* **2020**, 13, 1–49, https://doi.org/10.3390/ma13153441.
23. Weiss, D.; Rios, O.; Sims, Z. C.; Mccall, S.; Ott, R. Casting characteristics of high cerium content aluminum alloys. *Light Metals* **2017**, 205–211, http://link.springer.com/10.1007/978-3-319-51541-0.
24. Nguyen, R. T. et al. Anticipating impacts of introducing aluminum-cerium alloys into the United States automotive market. *Resour. Conserv. Recycl.* **2019**, 144, 340–349, 2019, https://doi.org/10.1016/j.resconrec.2019.02.009.
25. Salonitis, K.; Jolly, M.; Pagone, E.; Papanikolaou, M. Life-cycle and energy assessment of automotive component manufacturing: The dilemma between aluminum and cast iron. *Energies* **2019**, 12, https://doi.org/10.3390/en12132557.
26. Kozakevich, J. R.; Stroh, J.; Sediako,D.; Weiss, D. DSC thermal analysis of a near eutectic Al-Ce alloy with additions of Ni and Mn," *COM Light Met. (in press)*.
27. ASTM (2017) Standard Guide for Preparation of Metallographic Specimens. *ASTM International,* https://doi.org/10.1520/E0003-11R17.1.
28. Vandersluis, E.; Ravindran, R. Comparison of measurement methods for secondary dendrite arm spacing *Metallogr. Microstruct. Anal.* **2017**, 6, 89–94, https://doi.org/10.1007/s13632-016-0331-8.

29. Zhang, H.; Zhang, C.; Zhang, L.; Zhai, F.; Tian, J. Effect of Cu on the microstructure and the property of Al-Ce-Ni-Cu amorphous nano-composite materials. *Adv. Mater. Res.* **2013**, 624, 248–251, https://doi.org/10.4028/www.scientific.net/AMR.624.248.
30. Haghdadi, H.; Phillion, A. B.; Maijer, D. M. Microstructure characterization and thermal analysis of aluminum alloy B206 during solidification. *Metall. Mater. Trans. A Phys. Metall. Mater. Sci.* **2015**, 46, 2073–2081, https://doi.org/10.1007/s11661-015-2780-0.
31. Boettinger, W. J.; Kattner, U. R.; Moon, K. W.; Perepezko, J. H. DTA and heat-flux DSC measurements of alloy melting and freezing. In *Methods for Phase Diagram Determination*; Zhao, J. C.; Elsevier Ltd., 2007, pp. 151-221, doi: https://doi.org/10.1016/b978-008044629-5/50005-7.
32. ASTM (2015) E794 − 06 Standard test method for melting and crystallization temperatures by thermal," *ASTM International,* doi: https://doi.org/10.1520/E0794-06R18.2.
33. Gout, D.; Benbow, E.; Gourdon, O.; Miller, G. J. Crystallographic, electronic and magnetic studies of Ce4Ni 6Al23: A new ternary intermetallic compound in the cerium-nickel-aluminum phase diagram. *J. Solid State Chem.* **2003**, 174, 471–481, https://doi.org/10.1016/S0022-4596(02)00167-6.
34. Yang, Y. et al. Primary solidification of ternary compounds in Al-rich Al–Ce–Mn alloys. *J. Alloys Compd.* **2020**, 844, https://doi.org/10.1016/j.jallcom.2020.156048.
35. Coury, F. G.; Kiminami, C. S.; Botta, W. J.; Bolfarini, C.; Kaufman, M. J. Design and production of Al-Mn-Ce alloys with tailored properties. *Mater. Des.* **2016**, 110, 436–448, http://dx.doi.org/10.1016/j.matdes.2016.08.008.
36. Gordillo,M. A.; Cernatescu, I.; Aindow, T. T.; Watson, T. J.; Aindow, M. Phase stability in a powder-processed Al-Mn-Ce alloy. *J. Mater. Sci.* **2014**, 49, 3742–3754, https://doi.org/10.1007/s10853-014-8086-6.
37. Liu, X. J.; Ohnuma, J.; Kainuma, R.; Ishida, K. Thermodynamic assessment of the Aluminum-Manganese (Al-Mn) binary phase diagram *J. Phase Equilibria* **1999**, 20, 45–56, 1999, https://doi.org/10.1361/105497199770335938.
38. Mondolfo, L. F. Al–Mn Aluminum–Manganese system. In *Aluminum Alloys: Structures and Properties*, Butterworth-Heinemann, 1976, pp. 324–329, https://doi.org/10.1016/b978-0-408-70932-3.50054-1.
39. Mondolfo, L. F. Al–Ce–Mn Aluminum–Cerium–Manganese system. In *Aluminum Alloys: Structures and Properties*, Butterworth-Heinemann, 1976, pp. 470–471, https://doi.org/10.1016/B978-0-408-70932-3.50169-8.
40. Okamoto, H. Al-Ce (Aluminum-Cerium). *J. Phase Equilibria Diffus.* **2011**, 32, 392–393, https://doi.org/10.1007/s11669-011-9914-x.
41. Tang, C.; Du, Y.; Zhou, H. The phase equilibria of the Al-Ce-Ni system at 500 °C. *J. Alloys Compd.* **2009**, 470, 222–227, https://doi.org/10.1016/j.jallcom.2008.03.034.
42. Tang, C. et al. Experimental investigation of the Al-Ce-Ni system at 800 °C. *Intermetallics* **2008**, 16, 432–439, https://doi.org/10.1016/j.intermet.2007.12.003.
43. Raghavan, V. Al-Ce-Ni (Aluminum-Cerium-Nickel). *J. Phase Equilibria Diffus.* **2009**, 30, 265–267, https://doi.org/10.1007/s11669-009-9516-z.
44. Tang, C. et al. Correlation between thermodynamics and glass forming ability in the Al-Ce-Ni system. *Intermetallics* **2010**, 18, 900–906, 2010, doi: http://dx.doi.org/10.1016/j.intermet.2009.12.027.